Title
Oxygen Transport through Amorphous Cathode Coatings in Solid-State Batteries

Journal
Chemistry of Materials, 36(6)

ISSN
0897-4756

Authors
Cheng, Jianli
Peng, Xinxing
Zhang, Ya-Qian
et al.

Publication Date
2024-03-26

DOI
10.1021/acs.chemmater.3c02351

Peer reviewed

CHEMISTRY OF MATERIALS

Open Access

pubs.acs.org/cm

Article

Oxygen Transport through Amorphous Cathode Coatings in Solid-State Batteries

Jianli Cheng,[⊥] Xinxing Peng,[⊥] Ya-Qian Zhang,[⊥] Yaosen Tian, Tofunmi Ogunfunmi, Andrew Z. Haddad, Andrew Dopilka, Gerbrand Ceder,* Kristin A. Persson,* and Mary C. Scott*

Cite This: *Chem. Mater.* 2024, 36, 2642−2651

Read Online

ACCESS | Metrics & More | Article Recommendations | Supporting Information

ABSTRACT: All solid-state batteries (SSBs) are considered the most promising path to enabling higher energy-density portable energy, while concurrently improving safety as compared to current liquid electrolyte solutions. However, the desire for high energy necessitates the choice of high-voltage cathodes, such as nickel-rich layered oxides, where degradation phenomena related to oxygen loss and structural densification at the cathode surface are known to significantly compromise the cycle and thermal stability. In this work, we show, for the first time, that even in an SSB, and when protected by an intact amorphous coating, the $LiNi_{0.5}Mn_{0.3}Co_{0.2}O_2$ (NMC^{532}) surface transforms from a layered structure into a rocksalt-like structure after electrochemical cycling. The transformation of the surface structure of the $Li_3B_{11}O_{18}$ (LBO)-coated NMC^{532} cathode in a thiophosphate-based solid-state cell is characterized by high-resolution complementary electron microscopy techniques and electron energy loss spectroscopy. Ab initio molecular dynamics corroborate facile transport of O^{2-} in the LBO coating and in other typical coating materials. This work identifies that oxygen loss remains a formidable challenge and barrier to long-cycle life high-energy storage, even in SSBs with durable, amorphous cathode coatings, and directs attention to considering oxygen permeability as an important new design criteria for coating materials.

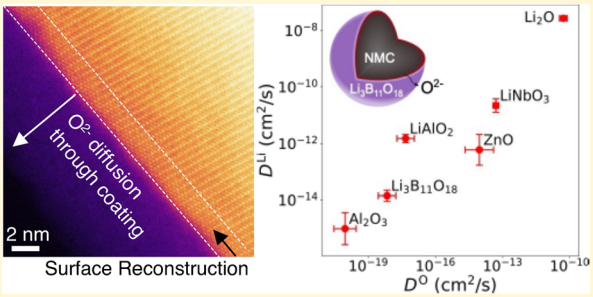

INTRODUCTION

The rising demand for long-range, safe, electrified transportation has highlighted the need for further advancements in rechargeable Li-ion batteries.[1−4] Currently, a promising technology to meet these goals is solid-state batteries (SSBs), which provide a safer solution to utilizing higher energy-density electrode materials. Such materials include a Li metal anode and a high-energy density cathode, often found in the family of Ni-rich layered cathodes $LiNi_xMn_yCo_{1-x-y}O_2$ (NMC, $x \geq 0.5$), owing to their high specific capacities and power densities. However, despite the many merits of Ni-rich layered cathodes, numerous studies have shown that when employed in liquid-electrolyte cells, at a high state of charge (SoC), electrochemical oxidation of oxygen and oxygen loss occur in the surface regions of the cathode, leading to destabilization of the transition metal cations at the surface.[5−8] This destabilization, in turn, leads to surface densification from the initial layered structure ($R\bar{3}m$) into an undesirable rocksalt-like ($Fm\bar{3}m$) or spinel-like ($Fd\bar{3}m$) structure.[7−10] The resulting structural degradation and interfacial mismatch with the underlying bulk material degrade lithium transport, causing impedance build-up, bulk fatigue,[1] and poor high-voltage cycling performance.

Indeed, the formation of a structural reconstruction layer (a reduced surface transition-metal layer) has been reported even after simply exposing NMC materials to $LiPF_6$-based organic electrolytic solutions.[11] The most prevalent strategy to protect the cathode surface in traditional liquid electrolyte cells is to coat the cathode with a protective "buffer" layer.[12−14] This layer typically comprises a solid ceramic[15−20] and to date, various surface coatings, including metal oxides (e.g., Al_2O_3, ZnO, Ta_2O_5),[16,17,21,22] metal fluorides (e.g., AlF_3),[19,20] and metal phosphates (e.g., $LaPO_4$)[17] have been shown to enhance the cyclability of NMC materials. However, recently, Zheng et al. reported that although the application of an AlF_3 coating on $Li_{1.2}Ni_{0.15}Co_{0.10}Mn_{0.55}O_2$ was found to protect the cathode surface from severe etching/corrosion and alleviated or delayed the surface reconstruction of the cathode compared with that without the coating, phase transformation from the layered to spinel-like structure still occurred after extended cycling.[19] Similarly, Croy et al.[23] reported that the use of an atomic layer-deposited Al_2O_3 coating as a physical barrier on a Ni-rich cathode was insufficient to overcome its surface

Received: September 13, 2023
Revised: February 24, 2024
Accepted: February 26, 2024
Published: March 14, 2024

instabilities. It is fair to conclude that cathode oxygen loss still occurs in liquid electrolyte cells and that the released oxygen may enhance electrolyte degradation, leading to the formation of high-impedance surface layers. Surprisingly, researchers have recently shown that similar surface structure reconstruction and transition metal reduction can be probed on a bare Ni-rich layered cathode when employed in a thiophosphate-based solid-electrolyte environment.[24] Ultimately, the final question is whether this surface structure rearrangement can be prohibited with the introduction of a stable, state-of-the-art surface coating[25] in SSBs.

In this work, we used high-resolution scanning transmission electron microscopy (STEM), transmission electron microscopy (TEM), and electron energy loss spectroscopy (EELS) complemented with ab initio molecular dynamics (AIMD) to investigate the surface structure evolution of a coated Ni-rich layered cathode in a thiophosphate-based SSB environment. An amorphous $Li_3B_{11}O_{18}$ (LBO) coating was selected as an example because, in previous work, it was observed and computed to be chemically/electrochemically stable even after extended cycling in an SSB.[26] In this work, we show that even when protected by an intact amorphous surface coating, the surface region of $LiNi_{0.5}Mn_{0.3}Co_{0.2}O_2$ (NMC^{532}) transforms from a layered structure into a rocksalt-like structure after electrochemical cycling in a SSB. More importantly, we demonstrate the essential role of O^{2-} transport in the ceramic coating. To date, surface coatings have been selected based on their facile Li-ion transport, low electron transport, chemical compatibility with both the SE and cathode, and electrochemical stability; however, oxygen transport in the coating material has never been considered as a criterion in their selection. We emphasize that if the surface coating exhibits a facile O^{2-} transport, the cathode can still lose oxygen, densify, and increase its impedance, even when coated by an amorphous surface coating. Using AIMD simulations, we systematically evaluated the O^{2-} diffusion rate in amorphous LBO as well as in other typical coating materials reported in the literature. The O^{2-} flux estimated using the Onsager transport models reveals facile transport of O^{2-} through amorphous LBO, rationalizing our observation that a rocksalt structure still forms on the surface of the NMC^{532} cathode in a solid-state cell. In summary, we provide the first evidence of the formation of a surface-reduced layer in NMC^{532} in the presence of an intact, amorphous oxide coating after cycling in a thiophosphate-based SSB. Our work highlights the importance of designing coating materials with a low O^{2-} diffusivity to mitigate cathode degradation, even in SSBs.

METHODS

Material Synthesis and Coating Method. The $Li_3B_{11}O_{18}$ (LBO)-coated $LiNi_{0.5}Mn_{0.3}Co_{0.2}O_2$ (NMC^{532}) samples were prepared by Samsung Research Japan using the sol−gel method reported in previous work.[26] For the LBO-coated NMC^{532} sample (0.5 mol % LBO coated NMC), the LBO coating solution was first prepared by dissolving a stoichiometric amount of Li acetate and triisopropyl borate in super dehydrated ethanol at 60 °C. Next, the NMC^{532} powder was dispersed in the as-prepared coating solution with stirring. Then, the solvent from the flask was removed using a rotary evaporator in a hot water bath (60 °C) with ultrasound sonication followed by a heat treatment at 350 °C in air. The $75Li_2S{-}25P_2S_5$ (LPS) was synthesized by ball-milling stoichiometric amounts of Li_2S (99.98% Sigma-Aldrich) and P_2S_5 (99% Sigma-Aldrich) in a 50 mL ZrO_2 jar for 200 min using a SPEX 8000 M mixer mill. The LPS with a small particle size used in the composite cathode was prepared by wet ball milling the LPS solid electrolyte (SE) with heptane and dibutyl ether using a Retsch PM200 ball mill for 40 h. All of the LPS synthesis steps were conducted in an Ar atmosphere.

Cell Fabrication and Electrochemical Characterization. SSBs were fabricated in an Ar-filled glovebox with H_2O < 2 ppm and O_2 < 0.1 ppm. The LPS, uncoated or LBO-coated NMC^{532}, and graphite were used as the SE, cathode, and anode active materials, respectively. The cathode and anode composites were prepared by hand mixing 60% active material, 35% LPS, and 5% CNF. The full cells were assembled using an in-house-designed pressure cell (13 mm inner diameter). First, 100 mg of LPS powder was added to the cell and cold pressed under ∼100 MPa pressure. Next, 10 mg of the cathode composite powders and anode composite powders were carefully spread evenly on the top and bottom sides of the LPS pellet, respectively. A pressure of ∼350 MPa was applied for 5 min to compact the cell and ensure good interfacial contact between the different components.[27−29]

All the electrochemical tests were conducted at room temperature under an Ar atmosphere, and a pressure of 5 MPa was applied to the cells during cycling. The full SSBs were cycled at a constant current (0.1 mA cm^{-2} for charge and 0.05 mA cm^{-2} for discharge) between 2.5 and 4.3 V versus Li/Li^+.

Electron Microscopy Experiments. The TEM sample preparation was conducted in an Ar-filled glovebox. The LBO-coated cathodes were extracted from the disassembled cells after cycling. The cycled and uncycled composite cathode powder samples were diluted in hexane and sonicated to obtain good particle dispersion. The TEM samples were prepared by drop casting the solution onto a copper mesh TEM grid with an ultrathin carbon and lacey carbon support. The TEM grids were transferred from the glovebox into the microscope under an inert Ar atmosphere using a Gatan 648 double-tilt vacuum-transfer holder. The high-resolution STEM and EELS analyses were performed using the TEAM I microscope (a modified FEI Titan 80−300 microscope with a double-aberration-corrected (scanning) transmission electron microscope) with an accelerating voltage of 300 kV.

For the EELS analysis, a power law background subtraction was performed for the Mn L_3/L_2 edge. Then, the multiple scattering was then removed by Fourier-ratio deconvolution using the low-loss spectrum obtained from the same scanning region using the dual EELS mode. To quantify the L_3/L_2 intensity ratio, a step function threshold with the ratio of step heights of 2:1 was first applied in the background subtraction to account for the multiplicity of the 3p1/2 and 3p3/2 initial states.[30] After the step function subtraction, the L_3/L_2 intensity ratios were determined by area integration beneath the L_3 and L_2 peaks.

Density Functional Theory Methods. All the density functional theory (DFT) electronic structure calculations were performed using the Vienna Ab initio Simulation Package[31] with projector-augmented wave potentials.[32] The Perdew−Burke−Ernzerhof generalized gradient approximation functional was adopted for the exchange−correlation functional.[33] For the AIMD simulations, we used Γ-point-only Brillouin zone integration at a plane-wave cutoff energy of 400 eV and a time step of 2 fs.

To generate the amorphous structures, we employed a "liquid-quench" process in which heating, equilibration, and quenching were performed using an AIMD workflow, which can be found as part of the open-source mpmorph package at http://github.com/materialsproject/mpmorph. We used the Packmol package[34] to generate the initial amorphous structures. To generate the "liquid" phase of the amorphous structures, the structures were "heated" at 3000 K, and a sequence of 4 ps AIMD simulations in the *NVT* ensemble was performed until the external pressure and energy converged. Then, the equilibrated "liquid" amorphous structures were simulated for an additional 10 ps, from which three independent configurations were selected, i.e., 3.3 ps apart from each other, and quenched to 0 K to obtain three, representative amorphous structures to exemplify varying atomic environments. The radial distribution functions of B−O, Al−O, and Nb−O pairs in $Li_3B_{11}O_{18}$, $LiAlO_2$, and $LiNbO_3$, respectively, at 0 K are plotted in Figure S1, which illustrates

https://doi.org/10.1021/acs.chemmater.3c02351
Chem. Mater. 2024, 36, 2642−2651

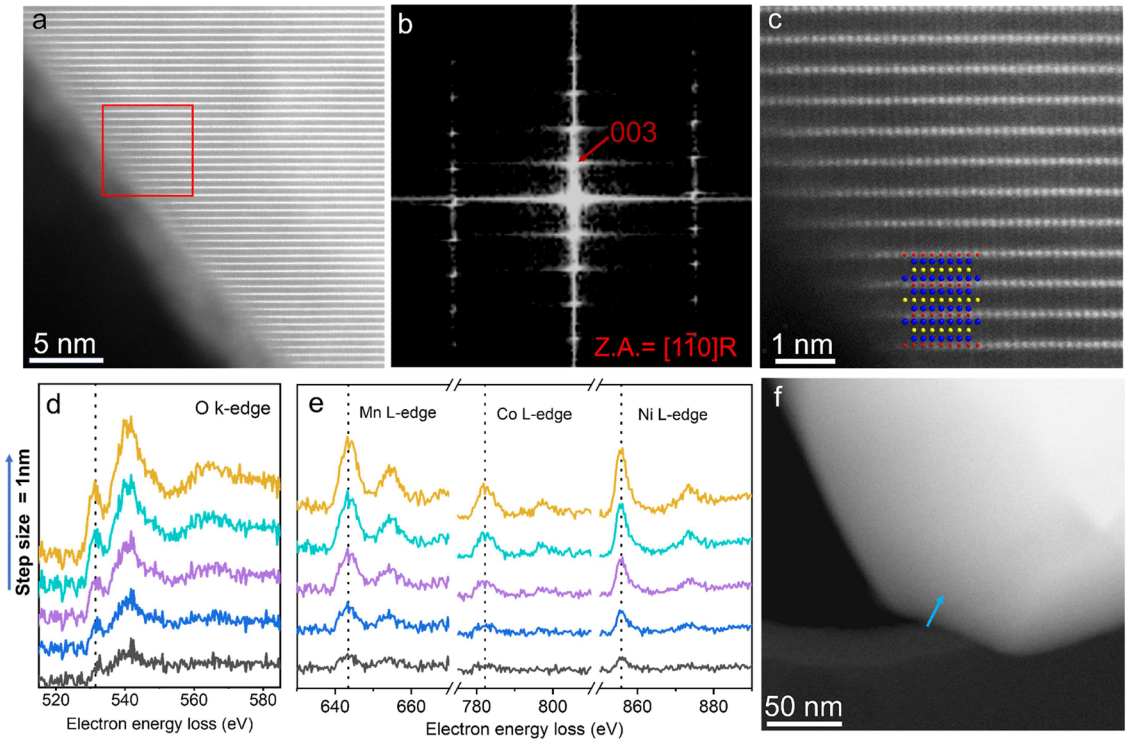

Figure 1. Structural characterization of the uncycled $Li_3B_{11}O_{18}$-coated $LiNi_{0.5}Mn_{0.3}Co_{0.2}O_2$ cathode composite. a, HAADF-STEM image of pristine LBO-NMC cathode composite. b, FFT image obtained from the selected surface region, showing the layered rhombohedral $R\bar{3}m$ structure along the [1−10] zone axis. c, Enlarged HAADF-STEM image of the surface region, confirming the well-defined layered structure prior to cycling. The inset image shows the ball models of NMC[532] viewing along [1−10]. The red, blue, and yellow balls represent mixed transition metal (Ni, Co, Mn), O and Li atoms. The d, e, EELS line scan spectra of (d) the O−K edge and (e) the Mn, Co, and Ni L-edge collected on pristine LBO-NMC cathode composite along the scanning pathway shown in the HAADF-STEM image in (f).

the distinct ordering behavior between amorphous and crystalline structures. For each configuration, we equilibrated the structures at T = 1800, 2000, 2200, 2400, 2600, and 2800 K, respectively, following the same procedure of obtaining the "liquid" amorphous structures mentioned above and then simulated an 80 ps diffusion trajectory at each corresponding temperature. Therefore, from the three representative amorphous structures, there are three independent diffusion trajectories at each corresponding temperature. Further details about the AIMD and DFT workflows can be found in ref.[13]

From the obtained diffusion trajectories, we calculated the self-diffusion coefficients (D) of Li^+ and O^{2-} ions using the Einstein relation: $D = d\langle\Delta r^2\rangle/6dt$, where t, r, and $\langle\Delta r^2\rangle$ are the time, ion position, and mean square displacement (MSD) that is averaged over all relevant ions (Li^+ or O^{2-} ions), respectively. Figure S2 illustrates the MSD of the Li^+ and O^{2-} ions in amorphous $Li_3B_{11}O_{18}$, $LiAlO_2$, and $LiNbO_3$. From this data, we obtained the D values at T = 1800, 2000, 2200, 2400, 2600, and 2800 K. At each temperature, there are three D values calculated from three independent AIMD diffusion trajectories obtained earlier for each representative amorphous structure. Figure S3 illustrates the density of the amorphous $Li_3B_{11}O_{18}$ structures versus the oxygen diffusivity (D^O). As expected, higher temperatures lead to a lower density due to an expanded volume, which in turn leads to an increase in oxygen diffusivity. The room-temperature D_{rt} were extrapolated from the D values at high temperatures using the Arrhenius relation, $D = D_0 \exp(-E_a/k_BT)$, where k_B is the Boltzmann constant, D_0 is the pre-exponential factor, and E_a is the activation energy of ion diffusion. D_0 and E_a were determined by fitting log D vs $1/T$ as the Arrhenius relation. Compared with the diffusion trajectories at higher temperatures (e.g., 2800 K), the trajectories at lower temperatures (e.g., 1800 K) typically exhibit fewer ion hops, thus yielding fitted D values with higher statistical uncertainty. Therefore, we considered the statistical uncertainty of the D value at each temperature when fitting the Arrhenius relation by assigning the standard deviation of log D as the uncertainty for each averaged D. In this study, the Arrhenius relation was fitted by the *curve_fit* function in the SciPy package.[35] It should be noted that pure B_2O_3 glass belongs to a strong glassformer, and its fragility increases with Li_2O content.[36−38] Therefore, even though the temperature-dependent D in $Li_3B_{11}O_{18}$ follows an Arrhenius-like relation at high temperatures, such as near the glass-transition temperature, it may not follow the same Arrhenius relation at low temperatures, such as room temperature. As a result, our estimated Li^+ and O^{2-} diffusivities in $Li_3B_{11}O_{18}$ could be overestimated. In addition, we fitted the temperature-dependent diffusivities with a non-Arrhenius Vogel−Fulcher−Tammann (VFT) equation[39] (see Figure S4), $D = D_0 e^{-E_a/k_B(T-T_0)}$, where T_0 is a temperature that is ∼50 K below the glass-transition temperature. However, because of the time limitations of AIMD simulations in calculating the diffusivities of $Li_3B_{11}O_{18}$ at low temperatures, i.e., 400−800 K, we are not able to obtain the fitted VFT equations with sufficient accuracy.

To estimate the ionic flux under the driving force of the chemical potential gradient across the coating layer, we applied the Onsager transport equation:

$$J^i = -L^{ii}\nabla\mu^i \tag{1}$$

where J^i, L^{ii}, and $\nabla\mu^i$ are the flux, Onsager transport coefficient, and chemical potential gradient of species i, respectively. It should be noted that in this study, we ignore the contributions from cross-correlations between two distinct species, such as L^{OLi}, and between distinct sites, such as $L^{OO}_{distinct}$, to J^O. Assuming steady-state conditions, we can reasonably approximate the chemical potential gradient $\nabla\mu^i$ to be a constant throughout the thickness of the coating, which renders the above equation as

$$J^i = L^{ii}\frac{\mu^i_c - \mu^i_e}{l_c} \tag{2}$$

https://doi.org/10.1021/acs.chemmater.3c02351
Chem. Mater. 2024, 36, 2642−2651

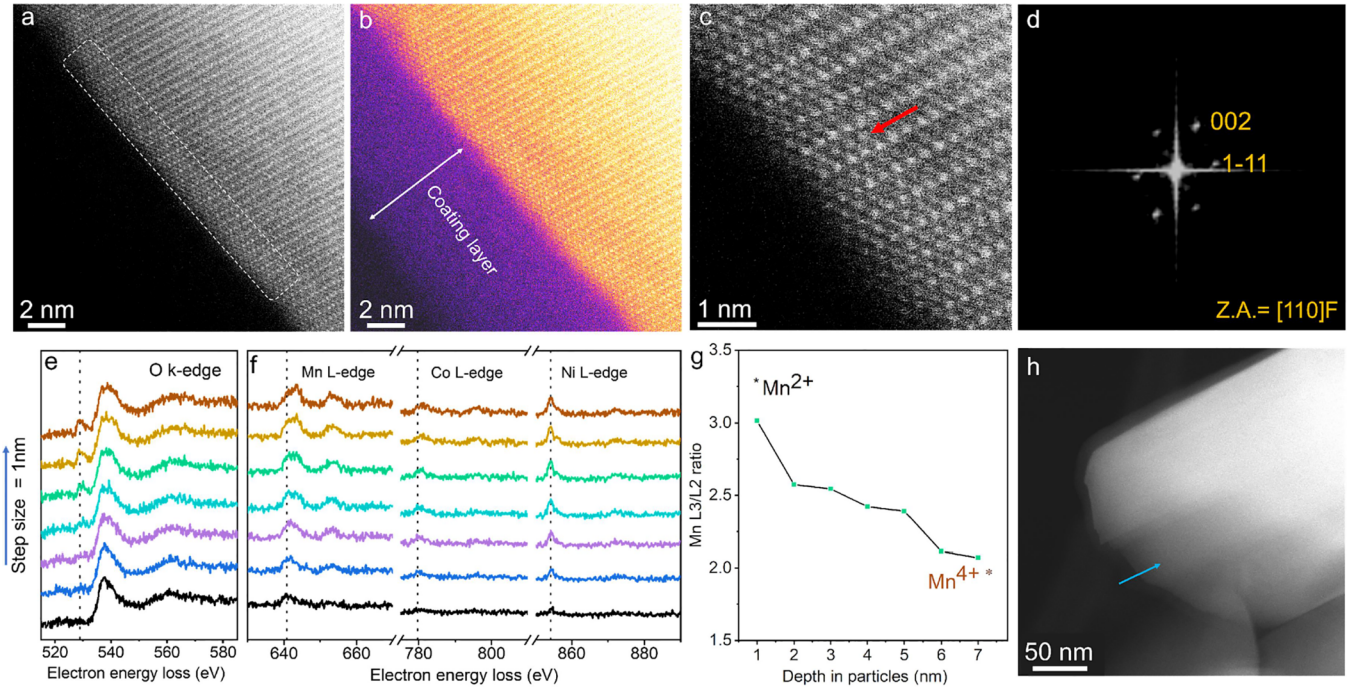

Figure 2. Structural characterization of cycled $Li_3B_{11}O_{18}$-coated $LiNi_{0.5}Mn_{0.3}Co_{0.2}O_2$. (a) HAADF-STEM image of LBO-NMC after cycling from 2.5 to 4.3 V versus Li for 10 cycles; (b) the same region displayed with false color for better visualization of the lithium borate thin-film coating. (c) Enlarged HAADF-STEM image of the surface region, showing the surface reconstruction layer. (d) FFT image obtained from the surface region, showing the $Fm\bar{3}m$ rocksalt structure along the [110] zone axis. (e, f) EELS line scan spectra of (e) O−K edge and (f) Mn, Co, and Ni L-edge collected on cycled LBO-NMC along the scanning pathway shown in (h). (g) L_3/L_2 intensity ratios of Mn L edges deduced from the EELS spectra in (f). h, HAADF-STEM image, showing the EELS line scan pathway.

where μ_c^i and μ_e^i are the chemical potentials at the cathode and electrolyte sides, respectively. Ignoring the $L_{distinct}^{ii}$ term, L^{ii} can be directly related to the self-diffusion coefficient D^i:

$$L^{ii} \approx L_{self}^{ii} = \frac{D^i c^i}{k_B T} = \frac{D_0^i e^{-E_a/k_B T} c^i}{k_B T} \quad (3)$$

where c^i is the concentration of species i in the coating. The room temperature L_{rt}^{ii} is extrapolated from L^{ii} values at high temperatures by fitting eq 3.

In this work, we estimate the time t required for O^{2-} to diffuse through the LBO coating in order to reach the observed surface rocksalt phase. We assume the surface rocksalt layer of the LBO-coated NMC^{532} mainly consists of NiO phase, which results from the surface NiO_2 to lose 50% of its oxygen. Let c_{max}^O denote the upper bound value of the O^{2-} concentration in NiO_2, and t can be calculated as

$$t = \frac{0.5 V c_{max}^O}{A J^O} \quad (4)$$

where A and V are the surface area of the LBO-coated NMC^{532} cathode particle and the shell volume of the surface rocksalt phase, respectively, and can be expressed as $V = \frac{4\pi}{3} r^3 - \frac{4\pi}{3}(r - l_s)^3$, $A = 4\pi(r + l_c)^2$, where r is the radius of the cathode particle, l_s is the thickness of the rocksalt phase, and l_c is the coating thickness. Combining eqs 2 and 4, we obtain

$$t = \frac{[r^3 - (r - l_s)^3]}{6(r + l_c)^2} \frac{c_{max}^O l_c}{L^{OO}(\mu_c^O - \mu_e^O)} \quad (5)$$

As $r \gg l_s$, l_c, the first term in eq 5 can be considered to be a constant for a given r. Therefore, the time t required to transport the same amount of O^{2-} through the LBO coating is mainly governed by the values of l_c and $\nabla\mu^O$. Hence, we consider a range of conditions to estimate t by varying the l_c and $\nabla\mu^O$.

RESULTS AND DISCUSSION

Appearance of a Surface-Reduced Layer in LBO-Coated NMC upon Cycling. We investigated LBO-coated $LiNi_{0.5}Mn_{0.3}Co_{0.2}O_2$ (LBO-NMC^{532}) from uncycled and cycled cathode composites (Figures S5−S10). The cathode composites were prepared by hand mixing 60% LBO-NMC, 35% $75Li_2S{-}25P_2S_5$ (LPS), and 5% CNF, with the cycled material undergoing 10 charge−discharge cycles from 2.5 to 4.3 V versus Li. The composite cathode material was then diluted in hexane and sonicated to obtain a good particle dispersion before drop casting on a TEM grid.

High-angle annular dark field scanning transmission electron microscopy (HAADF-STEM) images of the uncycled LBO-NMC along the [1−10] zone axis are presented in Figure 1a,c. The bright and dark regions in the HAADF-STEM images correspond to atomic columns of transition-metal cations and Li ions, respectively. Despite coming into contact with the amorphous LPS solid electrolyte (Figure S11), the HAADF-STEM image and corresponding fast-Fourier transform (FFT) image (Figure 1b) indicate that the uncycled nanoscale LBO-coated NMC maintains a well-defined $R\bar{3}m$ layered structure with separated transition metal and lithium sites in both the edge and bulk of the NMC particle (Figure S9).

Depth-profiled EELS line scan spectra collected on the surface of LBO-NMC from the cathode composite were used to probe the surface and bulk electronic structure of the uncycled LBO-NMC. The oxygen K-edge spectra shown in Figure 1d show a characteristic[40,41] pre-edge feature onset at ∼525 eV alongside the main edge at 532 eV, which corresponds to the promotion of O 1s electrons to hybridized TM3d-O 2p and TM4sp-O 2p orbitals.[42] The location and shape of these K-edge features are consistent from the surface

https://doi.org/10.1021/acs.chemmater.3c02351
Chem. Mater. 2024, 36, 2642−2651

to the bulk of the NMC, as are the L edges of the transition metals (Mn, Co, and Ni). These features suggest that the average oxidation states of the transition metal cations remain unchanged in the uncycled LBO-NMC after exposure to the solid-electrolyte thiophosphate environment in the composite cathode.

A similar analysis of cycled LBO-NMC reveals the presence of a thick rocksalt-like surface layer in the NMC (Figure 2a), despite the nanoscale LBO amorphous coating (Figures 2b, S10, and S12). High-resolution HAADF-STEM imaging (Figure 2a–c) shows the atomic cation arrangement on the surface of the cycled LBO-NMC along the [100] zone axis of the bulk layered rhombohedral $R\bar{3}m$ structure. Even with the protection of the LBO coating, cation mixing within a few atomic layers (~2 nm) is readily observed in the surface region of the cycled LBO-NMC (Figures S8 and S10). FFT analysis of the surface of the LBO-NMC after electrochemical cycling confirms that the surface region consists primarily of an $Fm\bar{3}m$ rock-salt-structured phase (Figure 2d). In addition, the STEM-EELS characterization of the cycled cathode composite confirms a fairly uniform distribution of oxygen in the SE after 10 cycles (Figure S13). Surface reconstruction of the cathode and a change in the oxidation state of the transition metal are observed after cycling (Figures 2a–h, S8, and S10), which supports the coating's O^{2-} permeability. The presence of oxygen is likely to oxidize Li_3PS_4, leading to the formation of a small amount of $P-O_x$ species.[43] Further evidence for the formation of a surface-reduced layer on the coated NMC is provided by EELS analysis of the cycled LBO-NMC (Figure 2e–h). As shown in the O K-edge spectra (Figure 2e), the pre-edge of the O K-edge in the surface region shows a significantly reduced intensity compared with that for the uncycled LBO-NMC or the inner region of the cycled NMC particle. Because the pre-edge intensity of the O K-edge strongly correlates with the density of available empty states in the hybridized metal 3d-O 2p orbitals in layered $LiTMO_2$,[42] the area under the oxygen pre-edge is generally found to show a linear correlation with the oxidation state of the TM (Mn, Co, Ni).[44,45] Thus, the significantly decreased pre-edge intensity on the surface of the cycled LBO-NMC suggests reduced oxidation states of the transition metals in the surface region of the LBO-NMC. The shift toward higher energy of the peak positions in the TM L edge peaks (particularly the Mn and Co L_3 peaks) at the surface (Figure 2f) also indicates reduced oxidation states near the surface of LBO-NMC after cycling. Quantitative analysis of the Mn L_3/L_2 edge intensity ratios in the cycled LBO-NMC shows that in the particle's bulk, the valence of Mn is 4^+, but is reduced to $\sim 2.2^+$ in the surface reconstruction region. The formation of a $Fm\bar{3}m$ rocksalt structure, the changes in the oxygen pre-edge intensities, and the shift of TM L-edge peaks in the HAADF-STEM and STEM-EELS profiles are all consistent with the presence of a densified surface area comprised of reduced cations on the LBO-coated layered NMC cathode after cycling.[6−8,11]

Confirmation of Ample Oxygen Mobility in Amorphous Coatings. To validate our hypothesis that oxygen diffusion plays a role in surface densification, we used ab initio methods to evaluate whether sufficient oxygen mobility is present in the coating materials to allow oxygen to escape from the layered cathode surface. We investigated the ionic diffusivity, flux, and transport time through the coating material using AIMD simulations and Onsager transport models. Because of the amorphous nature of the LBO and the typical coatings, we specifically targeted amorphous coatings in our calculations. The equilibrated amorphous structures were generated using a "liquid-quench" process, which was simulated using a series of AIMD calculations, as described in the Methods. From the AIMD-calculated diffusion trajectories, we extracted the self-diffusion coefficients and estimated the O^{2-} diffusion rate.

The room temperature self-diffusion coefficients of Li^+ (D^{Li}) and O^{2-} (D^O) in LBO are estimated by extrapolating the D values from high temperatures using the Arrhenius relation (Figure S14). For comparison, we also compute D^{Li} and D^O of two commonly used amorphous cathode coatings, $LiAlO_2$ and $LiNbO_3$, and include three previously calculated[13] amorphous Al_2O_3, ZnO, and Li_2O, see Figure 3. Figure S14 presents

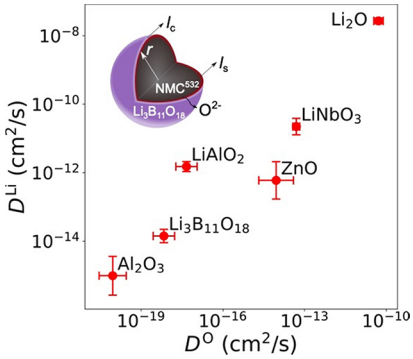

Figure 3. Self-diffusion coefficients in selected amorphous materials. Calculated room-temperature self-diffusion coefficients of Li^+ and O^{2-} in $Li_3B_{11}O_{18}$, Al_2O_3, $LiAlO_2$, ZnO, $LiNbO_3$, and Li_2O. The inserted figure shows the oxygen loss from the surface of the $Li_3B_{11}O_{18}$-coated NMC^{532}. r is the radius of an NMC^{532} particle, l_c is the coating thickness, and l_s is the thickness of the surface rocksalt phase. The error bars represent the standard deviation of extrapolated self-diffusion coefficients at 300 K. Amorphous 0.23 Li_2O·0.77 Al_2O_3 and 0.11 Li_2O·0.89 ZnO were used to simulate Li^+ and O^{2-}diffusion in Al_2O_3 and ZnO, respectively.

Arrhenius plots of the Li^+ and O^{2-} self-diffusivity D in $Li_3B_{11}O_{18}$, $LiAlO_2$, and $LiNbO_3$ as a function of temperature T. We note that Al_2O_3, $LiAlO_2$, $LiNbO_3$, and ZnO have all been reported to form an amorphous cathode coating and improve the cell cycling stability.[46−48] The calculated values for D^{Li} and D^O in LBO are 1×10^{-14} and 7×10^{-19} cm^2/s, respectively, both of which are lower than the respective values in $LiAlO_2$ and $LiNbO_3$. Tables 1 and 2 list the calculated activation energies E_a, D, and the Onsager transport coefficient L^{ii} of Li^+ and O^{2-} diffusion for the amorphous structures. More details on the calculation of L^{ii} can be found in the Methods. In Figure S15, we also plotted the calculated D^{Li} and D^O at 300 K in various $Li_xB_yO_z$ compositions among which LBO exhibits the smallest D^O.

We evaluate the effectiveness of the LBO coating in suppressing oxygen loss-induced surface reconstructions of the layered cathode by estimating the O^{2-} flux under steady-state conditions. To estimate the time t required for O^{2-} to diffuse through the LBO coating, we consider a range of conditions by varying the coating thickness (l_c) and oxygen chemical potential gradient ($\nabla\mu^O$). The oxygen chemical potential on the cathode side (μ_c^O) can be estimated from the cathode densification reaction consistent with the phase diagram. For example, at 4.3 V, layered NiO_2 would densify to rocksalt NiO, with oxygen being released at $\mu_c^O = -4.95$ eV.

https://doi.org/10.1021/acs.chemmater.3c02351
Chem. Mater. 2024, 36, 2642−2651

Table 1. Calculated Activation Energy E_a, Extrapolated Room-Temperature Diffusivity D, and Onsager Transport Coefficient L^{LiLi} for Li^+ Diffusion[a]

compounds	E_a^{Li} (eV)	D^{Li}(cm^2/s)	error bound D^{Li}	L^{LiLi} ($eV^{-1} \cdot cm^{-1} \cdot s^{-1}$)	error bound L^{LiLi}
$Li_3B_{11}O_{18}$	0.68 ± 0.03	1×10^{-14}	9×10^{-15}, 2×10^{-14}	6×10^{9}	4×10^{9}, 9×10^{9}
$LiAlO_2$	0.54 ± 0.02	2×10^{-12}	1×10^{-12}, 2×10^{-12}	1×10^{12}	9×10^{11}, 2×10^{12}
$LiNbO_3$	0.47 ± 0.03	2×10^{-11}	1×10^{-11}, 4×10^{-11}	1×10^{13}	8×10^{12}, 2×10^{13}
Al_2O_3	0.74 ± 0.08	1×10^{-15}	3×10^{-16}, 4×10^{-15}	5×10^{8}	1×10^{8}, 2×10^{9}
ZnO	0.58 ± 0.07	6×10^{-13}	2×10^{-13}, 2×10^{-12}	2×10^{11}	5×10^{10}, 7×10^{11}
Li_2O	0.26 ± 0.01	3×10^{-8}	2×10^{-8}, 3×10^{-8}	7×10^{16}	6×10^{16}, 9×10^{16}

[a]The error bars correspond to the standard deviation of activation energy from the Arrhenius relation. The error bounds correspond to the standard deviation of extrapolated diffusivities and transport coefficients at 300 K. Amorphous 0.23 Li_2O·0.77 Al_2O_3 and 0.11 Li_2O·0.89 ZnO were used to simulate Li^+ diffusion in Al_2O_3 and ZnO, respectively

Table 2. Calculated Activation Energy E_a, Extrapolated Room-Temperature Diffusivity D_{rt}, and Onsager Transport Coefficient L^{OO} for O^{2-} Diffusion[a]

compounds	E_a^{O} (eV)	D^{O} (cm^2/s)	error bound D^{O}	L^{OO} ($eV^{-1} \cdot cm^{-1} \cdot s^{-1}$)	error bound L^{OO}
$Li_3B_{11}O_{18}$	0.92 ± 0.05	7×10^{-19}	3×10^{-19}, 2×10^{-18}	1×10^{6}	5×10^{5},4×10^{6}
$LiAlO_2$	0.86 ± 0.05	5×10^{-18}	2×10^{-18}, 1×10^{-17}	9×10^{6}	3×10^{6},2×10^{7}
$LiNbO_3$	0.61 ± 0.02	5×10^{-14}	4×10^{-14}, 7×10^{-14}	9×10^{10}	7×10^{10},1×10^{11}
Al_2O_3	1.04 ± 0.07	9×10^{-21}	3×10^{-21}, 3×10^{-20}	2×10^{4}	5×10^{3},6×10^{4}
ZnO	0.67 ± 0.09	9×10^{-15}	2×10^{-15}, 4×10^{-14}	1×10^{10}	3×10^{9},6×10^{10}
Li_2O	0.37 ± 0.02	5×10^{-11}	3×10^{-11}, 8×10^{-11}	7×10^{13}	5×10^{13},1×10^{14}

[a]The error bars correspond to the standard deviation of the activation energy from the Arrhenius relation. The error bounds correspond to the standard deviation of extrapolated diffusivities and transport coefficients at 300 K. Amorphous 0.23 Li_2O·0.77 Al_2O_3 and 0.11 Li_2O·0.89 ZnO were used to simulate O^{2-} diffusion in Al_2O_3 and ZnO, respectively.

The estimate for the oxygen chemical potential on the electrolyte side (μ_e^O) depends on how the oxygen reacts on the electrolyte side of the coating. We evaluate two limiting conditions: (1) a lower bound for the chemical potential obtained from reaction of oxygen with the electrolyte to form a new oxidized compound (at $\mu_e^O = -8.39$ eV, Li_3PS_4 reacts with oxygen and forms Li_3PO_4); (2) an upper bound assuming oxygen loses electrons to the carbon network and is released as O_2 (at μ_e^O=−5.24 eV at room temperature and $P_e^{O_2} = 0.21$ atm). Therefore, the range of μ_e^O is assumed to be $-8.39 \leq \mu_e^O \leq -5.24$ eV. The O^{2-} concentration in NiO_2, denoted as c_{max}^O, is ≈4.2×10^{22} cm^{-3}. Thus, densification to NiO requires about 2.1×10^{22} cm^{-3} of O^{2-} to diffuse through the coating. Based on the experimental observations, we set the radius of the NMC^{532} cathode particle to $r = 5$ μm and the thickness of the surface rocksalt phase to be $l_s = 2$ nm. Finally, we estimated the time t required for the surface NiO_2 to lose 50% of its oxygen. Table 3 shows that the released oxygen can diffuse through the LBO coating in 1.4−165 min, depending on l_c and $\nabla\mu^O$. We emphasize that this time is considerably shorter than the time an electrode spends at high voltage, where its driving force for oxygen release is the highest.

Table 3. Estimated Time t for O^{2-} to Diffuse through the LBO Coating for Various l_c Values and $\nabla\mu^i$[a]

r (μm)	l_s (nm)	μ_c^O (eV)	μ_e^O (eV)	l_c (nm)	t (min)	error bound t
5	2	−4.95	−8.39	1	1.4	0.5, 3.8
				10	14	5, 38
			−5.24	1	16.6	6.5, 45
				10	165	64,452

[a]l_c is the LBO coating thickness. μ_c^O and μ_e^O are the oxygen chemical potentials on the cathode and electrolyte side, respectively. We assume an NMC^{532} cathode particle radius (r) of 5 μm that forms a surface layer of densified NiO rocksalt phase with thickness (l_s) of 2 nm.

Implications for Cathode Coating Design. In this article, we provide the first evidence of the formation of a surface-reduced layer in NMC^{532} in the presence of an amorphous LBO coating after cycling in a thiophosphate-based SSB. The fact that a reduced cation-disordered region forms at the surface of LBO-NMC^{532} indicates that the strategy of using a chemically/electrochemically stable amorphous surface coating with low electronic conductivity remains insufficient to inhibit the surface densification of the cathode particles, even in a SSB. We propose that the origin of the surface transformation of NMC^{532} in the presence of an amorphous coating originates in oxygen transport through the coating. Using AIMD and the Onsager transport model, we demonstrate that under a reasonable gradient range of oxygen chemical potential and coating thickness, transport of the O^{2-} through the LBO coating can indeed occur on the time scale of electrochemical cycling. Such oxygen loss triggers the formation of a densified rocksalt phase at the surface of NMC^{532}, even in the presence of an intact and amorphous surface coating. Besides increasing the impedance of the cathode, oxygen transport through the coating may damage the solid electrolyte by creating phases with lower conductivity or by mechanical decohesion related to the reaction-induced volume change.

As revealed by the modeling, the effectiveness of a surface coating in retaining oxygen in the cathode is determined by both kinetic and thermodynamic factors, primarily the oxygen diffusion rate in the coating materials and the oxygen chemical potential gradient across the coating layer. The high oxygen chemical potential of a charged cathode drives the O^{2-} to diffuse from the cathode surface to the SE. On the cathode surface side, O^{2-} can either lose electrons to the carbon network and be released as O_2 or react with the SE. In an SSB

https://doi.org/10.1021/acs.chemmater.3c02351
Chem. Mater. 2024, 36, 2642−2651

with a thiophosphate SE, the presence of oxygen is likely to oxidize Li_3PS_4.[49,50] Although previous research has shown that for an uncoated Ni-rich layered cathode, the surface oxygen loss and surface structure rearrangement is strongly correlated to the environmental conditions,[51] our calculations confirm that it is possible to create a surface reduced layer even when direct contact between the cathode and the SE is prevented by an amorphous coating. It is worth noting that although the amorphous LBO coating significantly improves the cycling performance of full SSBs compared with an uncoated NMC cathode (Figures S16 and S17), a capacity loss of ∼20% is still observed after 100 cycles. The reduced Li kinetics due to cathode surface densification and the oxidation of the surrounding thiophosphate SE all play roles in this performance degradation.

Although our key findings in this study are based on a thiophosphate system, we argue that oxygen diffusion in the coating material is broadly relevant in solid-electrolyte and liquid-electrolyte systems. For a solid electrolyte that does not react with oxygen, such as $Li_7La_3Zr_2O_{12}$, μ_e^O can be estimated from the oxygen partial pressure ($P_e^{O_2}$) of air at room temperature and therefore corresponds to the calculated upper bound of $\mu_e^O = -5.24$ eV. In this case, we find that the driving force for oxygen diffusion through the coating becomes smaller than in the case of a reactive SE such as Li_3PS_4. However, in this scenario, we still estimate that only 17−165 min is needed at a high state of charge for enough oxygen to diffuse through a 1−10 nm LBO coating to create a 2 nm fully densified layer. This diffusion time is comparable to the thiophosphate case and, in the context of SSB operation, is expected to occur within a few cycles.

To demonstrate the broader consequences of our findings, we extend our modeling to other reported coating materials. Following the same procedure and assumption outlined above, we determine O^{2-} transport through a 1−10 nm Al_2O_3 coating. We find that the O^{2-} diffusivity (D^O) and Onsager transport coefficient (L^{OO}) in Al_2O_3 are approximately 2 orders of magnitude less than those in an LBO coating (see Table 2). As a result, the estimated time t required to transport the same amount of O^{2-} through an Al_2O_3 coating varies between 2 and 230 h, depending on l_c and $\nabla\mu^O$ (see Table S1). Experimentally, Croy et al.[23] reported that Al_2O_3 surface coating is not sufficient to stabilize an NMC cathode surface, while David et al.[16] showed an Al_2O_3 ALD coating can effectively prevent surface reconstruction of an NMC cathode. Our calculations demonstrate that an NMC cathode coated with a thin Al_2O_3 coating layer, such as 1 nm, is still prone to surface oxygen loss, especially when cycled at a low C-rate. On the other hand, a thicker Al_2O_3 coating layer can effectively mitigate O^{2-} transport, which results in better cathode surface protection. In addition, our calculations show that the Li^+ and O^{2-} diffusivities in commonly used $LiAlO_2$ and $LiNbO_3$ coatings are higher than those of LBO, which suggests a faster oxygen loss should occur from $LiAlO_2$- or $LiNbO_3$-coated NMC. Other inorganic Li^+-containing compounds, such as Li_2CO_3, have been suggested as viable components in a protective surface coating layer due to their electronic insulating properties and overall acceptable ionic conductivity. A previous theoretical study has reported that the Li^+ diffusivity in Li_2CO_3 is $\sim 10^{-7}$ cm^2/s.[52] Given the correlated diffusion between Li^+ and O^{2-}, we approximate that Li_2CO_3 exhibits a similar O^{2-} diffusivity with Li_2O, $\sim 10^{-10}$ cm^2/s. It should be noted that our diffusion analysis neglects the reaction kinetics of surface structural transitions and back diffusion of transition metals whose effects contribute to the surface reconstruction into the densified layer.[9] The bulk region of the cathode particle remains as a layered phase due to the slow kinetics associated with the layered-to-spinel transition.[9]

Using ab initio calculations and the Onsager transport theory, we propose that oxygen transport in coating materials plays an essential role in the surface reconstruction and oxygen loss of the layered cathode in various coating and electrolyte systems. In addition to the criteria of providing facile Li^+ transport and preventing chemical reactions between the cathode and electrolyte, we highlight the importance of designing coating materials with low O^{2-} diffusivity to block oxygen diffusion and mitigate lattice densification at the cathode surface. However, based on the coating materials investigated in this study, we note that there can be a trade-off between the O^{2-} diffusivity and Li^+ diffusivity, as shown in Figure 3. Generally, the diffusion of Li^+ and O^{2-} are correlated.[14] This is because Li^+ is bonded to its neighboring O^{2-} ions, and its diffusion through the amorphous coating is governed by discrete hops between two adjacent sites, which are initiated by the Li−O bond breaking/formation process. Therefore, more sluggish O^{2-} diffusion generally accompanies a slower Li^+ diffusion. An ideal amorphous coating should maintain a low O^{2-} diffusivity and a high Li^+ diffusivity to achieve oxygen-retaining and surface-protective functions while avoiding significant losses in rate capacity. To guide the selection of coatings with adequate Li^+ diffusion as well as reasonably low O^{2-} diffusion, we refer to ref[14] which presents an extensive high-throughput computational study of 20 common coating materials and their self-diffusion coefficients.[14] In ref,[14] design guidelines for Li^+ and O^{2-} diffusivities are provided; specifically recommending that Li^+ diffusivity should be higher than 7×10^{-16} cm^2/s and O^{2-} diffusivity should be lower than 10^{-17} cm^2/s. In particular, it is reported that BO_x^{y-}, SiO_x^{y-}, PO_x^{y-}, and SbO_x^{y-} exhibit improved oxygen retention,[14] which focuses the attention on cathode coating materials that contain one or more of these anion groups.

CONCLUSIONS

In this work, we use STEM and EELS to conclusively show that even in an SSB, and when protected by an intact, amorphous coating, the surface of a high-energy density oxide cathode still transforms from a layered structure into a rock-salt-like structure after electrochemical cycling. We propose that the reason a stable surface coating cannot inhibit the cathode surface degradation lies in oxygen transport in the surface coating. Using AIMD calculations, we systematically evaluated the O^{2-} diffusion rate in amorphous LBO as well as in typical cathode coating materials reported in the literature. Our results demonstrate the facile O^{2-} transport through the LBO coating and explain similar surface densification observed in liquid-cell systems on coated layered oxide cathodes in the literature. This work identifies oxygen loss as a significant barrier to long-cycle life high-energy storage, even in SSBs with coated cathodes, and highlights the need to design durable, amorphous cathode coatings with optimized lithium/oxygen diffusivity.

https://doi.org/10.1021/acs.chemmater.3c02351
Chem. Mater. 2024, 36, 2642−2651

■ ASSOCIATED CONTENT

Data Availability Statement

All data needed to evaluate the conclusions in the paper are present in the paper and/or the Supporting Information.

Supporting Information

The Supporting Information is available free of charge at https://pubs.acs.org/doi/10.1021/acs.chemmater.3c02351.

Radial distribution functions, MSD of Li^+ and O^{2-} ions, density versus oxygen diffusivity, fitting diffusivities using VFT and Arrhenius equations, TEM images of the uncycled and cycled cathode, structural characterization of the uncycled and cycled cathode, X-ray diffraction pattern of LPS, thickness distribution of the LBO coating layer, composition characterization of the cycled cathode, Arrhenius plots of Li^+ and O^{2-} diffusivity, calculated room-temperature diffusivities of Li^+ and O^{2-}, cycling performance comparison, electrochemical cycling data, and estimated time for O^{2-} to diffuse through the Al_2O_3 coating (PDF)

Accession Codes

The codes used in this study are available either publicly (mpmorph; http://github.com/materialsproject/mpmorph) or through subscription (Vienna Ab-initio Simulation Package; https://www.vasp.at). For a detailed description of input parameters used for each code, refer to the "Density functional theory methods" section in the Methods.

■ AUTHOR INFORMATION

Corresponding Authors

Gerbrand Ceder − *Materials Sciences Division, Lawrence Berkeley National Laboratory, Berkeley, California 94720, United States; Department of Materials Science and Engineering, University of California at Berkeley, Berkeley, California 94720, United States;* orcid.org/0000-0001-9275-3605; Email: gceder@berkeley.edu

Kristin A. Persson − *Materials Sciences Division and The Molecular Foundry, Lawrence Berkeley National Laboratory, Berkeley, California 94720, United States; Department of Materials Science and Engineering, University of California at Berkeley, Berkeley, California 94720, United States;* orcid.org/0000-0003-2495-5509; Email: kapersson@lbl.gov

Mary C. Scott − *Department of Materials Science and Engineering, University of California at Berkeley, Berkeley, California 94720, United States; The Molecular Foundry, Lawrence Berkeley National Laboratory, Berkeley, California 94720, United States*; Email: mary.scott@berkeley.edu

Authors

Jianli Cheng − *Materials Sciences Division, Lawrence Berkeley National Laboratory, Berkeley, California 94720, United States;* orcid.org/0000-0002-0302-7861

Xinxing Peng − *Department of Materials Science and Engineering, University of California at Berkeley, Berkeley, California 94720, United States; The Molecular Foundry, Lawrence Berkeley National Laboratory, Berkeley, California 94720, United States;* orcid.org/0000-0002-7077-8454

Ya-Qian Zhang − *Department of Materials Science and Engineering, University of California at Berkeley, Berkeley, California 94720, United States; The Molecular Foundry, Lawrence Berkeley National Laboratory, Berkeley, California 94720, United States*

Yaosen Tian − *Materials Sciences Division, Lawrence Berkeley National Laboratory, Berkeley, California 94720, United States; Department of Materials Science and Engineering, University of California at Berkeley, Berkeley, California 94720, United States*

Tofunmi Ogunfunmi − *Department of Materials Science and Engineering, University of California at Berkeley, Berkeley, California 94720, United States*

Andrew Z. Haddad − *Energy Storage and Distributed Resources Division, Lawrence Berkeley National Laboratory, Berkeley, California 94720, United States;* orcid.org/0000-0002-9206-3505

Andrew Dopilka − *Energy Storage and Distributed Resources Division, Lawrence Berkeley National Laboratory, Berkeley, California 94720, United States*

Complete contact information is available at: https://pubs.acs.org/10.1021/acs.chemmater.3c02351

Author Contributions

[⊥]J.C., X.P., and Y.-Q.Z.: co-authorship.

Author Contributions

G.C., K.A.P., and M.S. planned the project and supervised all aspects of the research. Y.-Q.Z., X.P., and J.C. contributed equally to this work. Y.-Q.Z., X.P., T.O., A.H., and A.D. designed the experiment and collected and analyzed the high-resolution STEM, TEM, EELS, and X-ray diffraction data. J.C. performed AIMD calculations. Y.T. fabricated the cells and performed the electrochemical cycling test.

Notes

The authors declare no competing financial interest.

■ ACKNOWLEDGMENTS

We acknowledge support from the Samsung Advanced Institute of Technology. The STEM and EELS experiments were performed at the Molecular Foundry, LBNL. Work at the Molecular Foundry was supported by the Office of Science, Office of Basic Energy Sciences, of the U.S. Department of Energy under Contract No. DE-AC02-05CH11231. The authors also gratefully acknowledge Dr. Taku Watanabe, Dr. Yuichi Aihara, Dr. Tomoyuki Tsujimura, and the Samsung R&D Institute of Japan for providing the LBO-coated cathode materials.

■ REFERENCES

(1) Xu, C.; et al. Bulk fatigue induced by surface reconstruction in layered Ni-rich cathodes for Li-ion batteries. *Nat. Mater.* **2021**, *20*, 84−92. (2020).

(2) Tian, Y.; et al. Promises and Challenges of Next-Generation 'beyond Li-ion' Batteries for Electric Vehicles and Grid Decarbonization. *Chem. Rev.* **2021**, *121*, 1623−1669.

(3) Li, W.; Zhu, J.; Xia, Y.; Gorji, M. B.; Wierzbicki, T. Data-Driven Safety Envelope of Lithium-Ion Batteries for Electric Vehicles. *Joule* **2019**, *3*, 2703−2715.

(4) Cheng, J.; Ouyang, B.; Persson, K. A. Mitigating the High-Charge Detrimental Phase Transformation in LiNiO2 Using Doping Engineering. *ACS Energy Lett.* **2023**, *8*, 2401−2407.

(5) Cheng, J.; et al. Enhancing surface oxygen retention through theory-guided doping selection in Li1−xNiO2 for next-generation lithium-ion batteries. *J. Mater. Chem. A Mater.* **2020**, *8*, 23293−23303.

(6) Armstrong, A. R.; et al. Demonstrating Oxygen Loss and Associated Structural Reorganization in the Lithium Battery Cathode Li [Ni Li Mn] O. *J. Am. Chem. Soc.* **2006**, *128*, 8694−8698.

(7) Tran, N.; et al. Mechanisms associated with the 'plateau' observed at high voltage for the overlithiated Li1.12(Ni0.425Mn 0.425Co0.15)0.88O2 system. *Chem. Mater.* **2008**, *20*, 4815−4825.
(8) Boulineau, A.; Simonin, L.; Colin, J. F.; Bourbon, C.; Patoux, S. First evidence of manganese-nickel segregation and densification upon cycling in Li-rich layered oxides for lithium batteries. *Nano Lett.* **2013**, *13*, 3857−3863.
(9) Xiao, P.; Shi, T.; Huang, W.; Ceder, G. Understanding surface densified phases in Ni-rich layered compounds. *ACS Energy Lett.* **2019**, *4*, 811−818.
(10) Yu, Z.; et al. Synthesis and Mechanism of High Structural Stability of Nickel-Rich Cathode Materials by Adjusting Li-Excess. *ACS Appl. Mater. Interfaces* **2020**, *12*, 40393−40403.
(11) Lin, F.; et al. Surface reconstruction and chemical evolution of stoichiometric layered cathode materials for lithium-ion batteries. *Nat. Commun.* **2014**, *5* (1), 3259.
(12) Xiao, Y.; Miara, L. J.; Wang, Y.; Ceder, G. Computational Screening of Cathode Coatings for Solid-State Batteries. *Joule* **2019**, *3*, 1252−1275.
(13) Cheng, J.; Sivonxay, E.; Persson, K. A. Evaluation of Amorphous Oxide Coatings for High-Voltage Li-Ion Battery Applications Using a First-Principles Framework. *ACS Appl. Mater. Interfaces* **2020**, *12*, 35748−35756.
(14) Cheng, J.; Fong, K. D.; Persson, K. A. Materials design principles of amorphous cathode coatings for lithium-ion battery applications. *J. Mater. Chem. A Mater.* **2022**, *10*, 22245−22256.
(15) (2018). Hu, E.; et al. Evolution of redox couples in Li- and Mn-rich cathode materials and mitigation of voltage fade by reducing oxygen release. *Nature Energy* **2018**, *3* (8), 690−698.
(16) David, L.; et al. Unveiling the Role of Al2O3 in Preventing Surface Reconstruction during High-Voltage Cycling of Lithium-Ion Batteries. *ACS Appl. Energy Mater.* **2019**, *2*, 1308−1313.
(17) Xiong, D. J.; Hynes, T.; Ellis, L. D.; Dahn, J. R. Effects of Surface Coating on Gas Evolution and Impedance Growth at Li[Ni x Mn y Co 1-x-y]O 2 Positive Electrodes in Li-Ion Cells. *J. Electrochem. Soc.* **2017**, *164*, A3174−A3181.
(18) Wise, A. M.; et al. Effect of Al2O3 Coating on Stabilizing LiNi0.4Mn0.4Co0.2O2 Cathodes. *Chem. Mater.* **2015**, *27*, 6146−6154.
(19) Zheng, J.; et al. Functioning mechanism of AlF3 coating on the Li- and Mn-rich cathode materials. *Chem. Mater.* **2014**, *26*, 6320−6327.
(20) Zheng, J. M.; et al. The Effects of AlF3 Coating on the Performance of Li [Li0.2Mn0.54Ni0.13Co0.13] O2 Positive Electrode Material for Lithium-Ion Battery. *J. Electrochem. Soc.* **2008**, *155*, A775.
(21) Kong, J. Z.; et al. Ultrathin ZnO coating for improved electrochemical performance of LiNi0.5Co0.2Mn0.3O2 cathode material. *J. Power Sources* **2014**, *266*, 433−439.
(22) Zhang, X.; et al. Improving the Structure Stability of LiNi0.8Co0.15Al0.05O2by Double Modification of Tantalum Surface Coating and Doping. *ACS Appl. Energy Mater.* **2021**, *4*, 8641−8652.
(23) Croy, J. R.; et al. Insights on the Stabilization of Nickel-Rich Cathode Surfaces: Evidence of Inherent Instabilities in the Presence of Conformal Coatings. *Chem. Mater.* **2019**, *31*, 3891−3899.
(24) Li, X.; et al. Unravelling the Chemistry and Microstructure Evolution of a Cathodic Interface in Sulfide-Based All-Solid-State Li-Ion Batteries. *ACS Energy Lett.* **2019**, *4*, 2480−2488.
(25) Li, J.; et al. The Impact of Electrolyte Additives and Upper Cut-off Voltage on the Formation of a Rocksalt Surface Layer in LiNi 0.8 Mn 0.1 Co 0.1 O 2 Electrodes. *J. Electrochem. Soc.* **2017**, *164*, A655−A665.
(26) Zhang, Y. Q.; et al. Direct Visualization of the Interfacial Degradation of Cathode Coatings in Solid State Batteries: A Combined Experimental and Computational Study. *Adv. Energy Mater.* **2020**, *10*, No. 1903778.
(27) Doux, J. M.; et al. Pressure effects on sulfide electrolytes for all solid-state batteries. *J. Mater. Chem. A Mater.* **2020**, *8*, 5049−5055.
(28) Zhang, J.; et al. All-solid-state batteries with slurry coated LiNi0.8Co0.1Mn0.1O2 composite cathode and Li6PS5Cl electrolyte: Effect of binder content. *J. Power Sources* **2018**, *391*, 73−79.
(29) Yubuchi, S.; et al. Preparation of high lithium-ion conducting Li6PS5Cl solid electrolyte from ethanol solution for all-solid-state lithium batteries. *J. Power Sources* **2015**, *293*, 941−945.
(30) Pearson, D. H.; Fultz, B.; Ahn, C. C. Measurements of 3d state occupancy in transition metals using electron energy loss spectrometry. *Appl. Phys. Lett.* **1988**, *53*, 1405−1407.
(31) Kresse, G.; Furthmüller, J. Efficient iterative schemes for *ab initio* total-energy calculations using a plane-wave basis set. *Phys. Rev. B* **1996**, *54*, 11169.
(32) Kresse, G.; Joubert, D. From ultrasoft pseudopotentials to the projector augmented-wave method. *Phys. Rev. B* **1999**, *59*, 1758.
(33) Perdew, J. P.; Burke, K.; Ernzerhof, M. Generalized Gradient Approximation Made Simple. *Phys. Rev. Lett.* **1996**, *77*, 3865.
(34) Martinez, L.; Andrade, R.; Birgin, E. G.; Martínez, J. M. PACKMOL: A package for building initial configurations for molecular dynamics simulations. *J. Comput. Chem.* **2009**, *30*, 2157−2164.
(35) (2020). Virtanen, P.; et al. SciPy 1.0: fundamental algorithms for scientific computing in Python. *Nat. Methods* **2020**, *17* (3), 261−272.
(36) Kojima, S.; Novikov, V. N.; Kodama, M. Fast relaxation, boson peak, and anharmonicity in Li2O−B2O3 glasses. *J. Chem. Phys.* **2000**, *113*, 6344−6350.
(37) Matsuda, Y.; Fukawa, Y.; Kawashima, M.; Kojima, S. Fragility Variation of Lithium Borate Glasses Studied by Temperature-Modulated DSC. *AIP Conf. Proc.* **2008**, *982*, 207−210.
(38) Chryssikos, G. D.; et al. Lithium borate glasses: a quantitative study of strength and fragility. *J. Non Cryst. Solids* **1994**, *172*−*174*, 378−383.
(39) (2020). Zhao, Q.; Stalin, S.; Zhao, C. Z.; Archer, L. A. Designing solid-state electrolytes for safe, energy-dense batteries. *Nature Reviews Materials* **2020**, *5* (3), 229−252.
(40) Carroll, K. J.; et al. Probing the electrode/electrolyte interface in the lithium excess layered oxide Li1.2Ni0.2Mn0.6O2. *Phys. Chem. Chem. Phys.* **2013**, *15*, 11128−11138.
(41) Hwang, S.; et al. Determination of the mechanism and extent of surface degradation in Ni-based cathode materials after repeated electrochemical cycling. *APL Mater.* **2016**, *4*, No. 096105, DOI: 10.1063/1.4963723.
(42) Yoon, W. S.; et al. Investigation of the charge compensation mechanism on the electrochemically Li-ion deintercalated Li1-xCo1/3Ni1/3Mn 1/3O2 electrode system by combination of soft and hard X-ray absorption spectroscopy. *J. Am. Chem. Soc.* **2005**, *127*, 17479−17487.
(43) Koerver, R.; et al. Capacity Fade in Solid-State Batteries: Interphase Formation and Chemomechanical Processes in Nickel-Rich Layered Oxide Cathodes and Lithium Thiophosphate Solid Electrolytes. *Chem. Mater.* **2017**, *29*, 5574−5582.
(44) House, R. A.; et al. Lithium manganese oxyfluoride as a new cathode material exhibiting oxygen redox. *Energy Environ. Sci.* **2018**, *11*, 926−932.
(45) House, R. A.; et al. What Triggers Oxygen Loss in Oxygen Redox Cathode Materials? *Chem. Mater.* **2019**, *31*, 3293−3300.
(46) Zhang, X.; et al. Structural and Electrochemical Study of Al2O3 and TiO2 Coated Li1.2Ni0.13Mn0.54Co0.13O2 Cathode Material Using ALD. *Adv. Energy Mater.* **2013**, *3*, 1299−1307.
(47) Park, J. S.; et al. Ultrathin lithium-ion conducting coatings for increased interfacial stability in high voltage lithium-ion batteries. *Chem. Mater.* **2014**, *26*, 3128−3134.
(48) Zhao, J.; Wang, Y. Ultrathin surface coatings for improved electrochemical performance of lithium ion battery electrodes at elevated temperature. *J. Phys. Chem. C* **2012**, *116*, 11867−11876.
(49) Bartsch, T.; et al. Gas Evolution in All-Solid-State Battery Cells. *ACS Energy Lett.* **2018**, *3*, 2539−2543.

(50) Walther, F.; et al. Influence of Carbon Additives on the Decomposition Pathways in Cathodes of Lithium Thiophosphate-Based All-Solid-State Batteries. *Chem. Mater.* **2020**, *32*, 6123−6136.
(51) Karki, K.; et al. Tuning the Activity of Oxygen in LiNi0.8Co0.15Al0.05O2 Battery Electrodes. *ACS Appl. Mater. Interfaces* **2016**, *8*, 27762−27771.
(52) Shi, S.; Qi, Y.; Li, H.; Hector, L. G. Defect thermodynamics and diffusion mechanisms in Li2CO 3 and implications for the solid electrolyte interphase in Li-ion batteries. *J. Phys. Chem. C* **2013**, *117*, 8579−8593.

https://doi.org/10.1021/acs.chemmater.3c02351
Chem. Mater. 2024, 36, 2642−2651